electronics

MDPI

Article

Robust DC-Link Voltage Tracking Controller with Variable Control Gain for Permanent Magnet Synchronous Generators

Seok-Kyoon Kim [1] and Kyo-Beum Lee [2,*]

[1] Seok-Kyoon Kim is with the Department of Creative Convergence Engineering, Hanbat National University, Daejeon 341-58, Korea; lotus45kr@gmail.com

[2] Kyo-Beum Lee is with the Department of Electrical and Computer Engineering, Ajou University, Suwon 443-749, Korea

* Correspondence: kyl@ajou.ac.kr; Tel.: +82-031-219-2376

Received: 9 October 2018; Accepted: 16 November 2018; Published: 21 November 2018

Abstract: This study develops a robust DC-link voltage tracking controller with variable control gain for permanent magnet synchronous generators. The first feature is to suggest an auto-tuning algorithm to drive the control gain to update the closed-loop cut-off frequency. The second one is to prove that the proposed controller incorporating auto-tuner and disturbance observer (DOB) coerces the closed-loop system to achieve the desired voltage tracking behavior, exponentially, with the steady-state rejection property. The control performance is demonstrated by emulating a wind-turbine power system using the powerSIM (PSIM) software.

Keywords: PMSG; DC-link voltage control; variable control gain; disturbance observer

1. Introduction

Nowadays, owing to major advantages such as high power density and efficiency, the permanent magnet synchronous machines (PMSMs) have rapidly replaced induction machines (IMs) for a wide range of industrial applications, including wind power systems [1–7]. The elimination of rotor excitation results in a considerable simplification of the machine structure and control algorithm.

PMSMs can be used as generators in various industrial applications, such as wind power systems and electric vehicles, and these generators are called permanent magnet synchronous generators (PMSGs). A PMSG connected to an external mechanical system acts as a power source with variable magnitude and frequency. The three-phase inverter has to be controlled to convert the AC power coming from a PMSG to the desired DC power, which can be viewed as an AC/DC conversion system with a several power source. The previous control techniques for AC/DC converters can be utilized for PMSG DC-link voltage control applications with a slight modification. Cascade-type controllers are commonly adopted for regulating the DC-link voltage of AC/DC converters as they provide better closed-loop performance than single-loop type controllers [8,9]. A cascade-type control system has current and voltage regulators in the inner- and outer-loops, respectively. Conventionally, both the inner- and outer-loops have been realized using the proportional-integral (PI) regulators with well-tuned PI gains through trial-and-error procedures. Bode and Nyquist methods have also been used to find a reasonable PI gain to achieve the desired specification given in the frequency domain, for a specified operating point. To cover an operating region, these techniques must be repeatedly applied for each operating point. The resulting PI gains need to be assigned to a closed-loop system through an additional gain scheduling algorithm as in [10]. The feedback-linearization (FL) controller was devised to overcome this drawback; it introduces a parameter-dependent additional feed-forward

compensator with PI gains [8,11,12]. The resulting closed-loop transfer function is obtained in the form of a first-order low-pass filter (LPF) with the desired cut-off frequency in the absence of model-plant mismatches. The reduction in parameter dependence was accomplished through passivity approaches [13–15], which inject a fixed damping effect to the closed-loop after shaping the desired energy function using partial converter parameter information. The same advantages can be obtained by using the adaptive [16] and sliding mode techniques [17]. There have been several attempts to incorporate the disturbance observers (DOBs) into classical PI controllers [18,19] for a better transient performance. A novel proportional-type controller embedding DOBs was suggested with a fixed closed-loop cut-off frequency for PMSG output voltage control applications [20]. The predictive techniques seek to achieve optimal control command for each control period by predicting the future state variable behavior, where the discretized dynamical equation with converter parameter values is used to predict the converter state [21,22]. The closed-loop performance driven by the extant parameter-dependent controllers could be improved by embedding an additional parameter identification mechanism as in [23–25] into the controller. Moreover, it is desirable to update the control gain automatically for a desirable cut-off frequency leading to a better closed-loop performance during transient periods.

This paper provides an auto-tuner-based robust DC-link voltage tracking controller for PMSGs driven by external mechanical systems. The parameter and load variation problems are handled by considering the perturbed dynamical model and adopting properly designed DOBs. The contributions are twofold: (a) the introduction of a closed-loop cut-off frequency update mechanism by the use of the variable control gain from the proposed auto-tuner (b) a rigorous closed-loop analysis for convergence and performance recovery without steady-state errors in the absence of tracking error integrators. Numerical verifications are conducted to demonstrate the effectiveness of the proposed controller by simulating the DC power supply system driven by a PMSG with wind turbines. The powerSIM (PSIM) software is used to emulate the wind power system, with the controller implemented using a dynamic link library (DLL).

2. PMSG Dynamics in Rotating *d-q* Axis

The time-varying coordinate transformation aligned to the electrical speed of PMSGs leads to the dynamical equations described in rotating *d-q* axis as [26]:

$$\mathbf{L}_{dq}\dot{\mathbf{i}}_{dq}(t) = -R_s\mathbf{i}_{dq}(t) + \mathbf{p}(\mathbf{i}_{dq}(t))\omega_r(t) + \mathbf{u}(t), \quad (1)$$

$$J\dot{\omega}(t) = -B\omega(t) + T_m(t) - T_e(i_d(t), i_q(t)),\ \forall t \geq 0, \quad (2)$$

where $\mathbf{i}_{dq}(t) := \begin{bmatrix} i_d(t) & i_q(t) \end{bmatrix}^T$ and $\mathbf{u}(t) := \begin{bmatrix} u_d(t) & u_q(t) \end{bmatrix}^T$ represent the state and control input vectors whose component correspond to the *d-q* axis current and terminal voltages. The nonlinearity of $\mathbf{p}(\mathbf{i}_{dq}(t))\omega_r(t)$ acts as a disturbance to the current dynamics of (1) where $\mathbf{p}(\mathbf{i}_{dq}(t)) := \begin{bmatrix} L_q i_q(t) & -(L_d i_d(t) + \lambda_{PM}) \end{bmatrix}^T$ and $\omega_r(t) := P\omega(t)$ with P being the pole pair. In the mechanical dynamics of (2), the mechanical speed is represented as $\omega(t)$ in rad/s, and external mechanical and electrical torques are denoted as $T_m(t)$ and $T_e(t)$ where $T_e(i_d(t), i_q(t)) := \frac{3}{2}P\Big(\Delta L_{dq} i_d(t) i_q(t) + \lambda_{PM} i_q(t)\Big)$, $\forall t \geq 0$, with $\Delta L_{dq} := L_d - L_q$. The electrical and mechanical machine parameters are given as follows: the *d-q* inductance of L_x, $x = d, q$, stator resistance of R_s, magnet flux of λ_{PM}, viscous damping of B, and rotor inertia of J.

Figure 1 depicts a DC power supply system driven by a PMSG with an external mechanical torque where $P_{in}(t)$, $P_{cap}(t)$, and $P_{grid}(t)$ denote the input power, output capacitor power, and grid power, respectively. These power signals are related as

$$P_{cap}(t) = Cv_{dc}(t)\frac{dv_{dc}(t)}{dt} = P_{in}(t) - P_{grid}(t),\ \forall t \geq 0. \quad (3)$$

By combining the relationship of $P_{in}(t) = P_G(t) - P_{loss,inv}(t)$, $\forall t \geq 0$, with the PMSG power of $P_G(t)$ and inverter power loss of $P_{inv,loss}(t)$, the equation of (3) gives

$$C\dot{v}_{dc}(t) = \frac{\omega(t)}{v_{dc}(t)} T_e(t) - \frac{P_{loss,inv}(t)}{v_{dc}(t)} - i_{grid}(t), \ \forall t \geq 0, \tag{4}$$

with $i_{grid}(t)$ denoting the load current toward the grid.

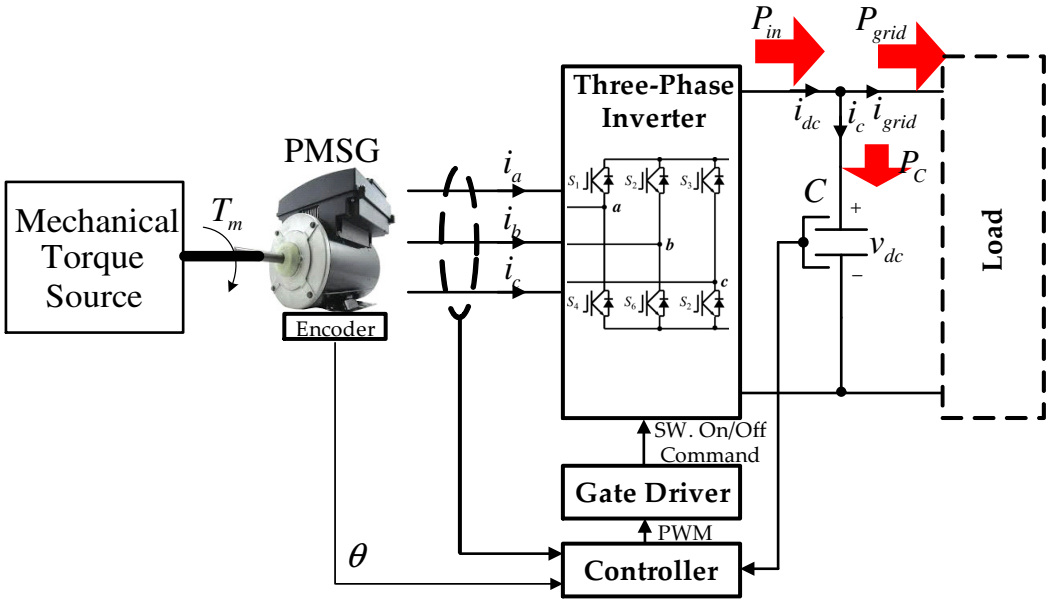

Figure 1. PMSG power system configuration.

For the system depicted in Figure 1, the d-q axis current of $i_x(t)$, $x = d, q$, and the DC-link voltage of $v_{dc}(t)$ are treated as state-variables for feedback, and the d-q axis PMSG terminal voltage of $u_x(t)$, $x = d, q$, correspond to the control input to be designed later. The system parameters of L_x, $x = d, q$, λ_{PM}, C, inverter power loss of $P_{loss,inv}(t)$, and load current of $i_{grid}(t)$ are assumed to be unknown because they can be varied significantly depending on the operating conditions.

3. DC-Link Voltage Controller Design

The goal of this section is to develop a control algorithm such that

$$\lim_{t \to \infty} v_{dc}(t) = v_{dc}^*(t), \tag{5}$$

exponentially, where the target trajectory of $v_{dc}^*(t)$ satisfies the LPF:

$$\dot{v}_{dc}^*(t) = \omega_{vc}(v_{dc,ref}(t) - v_{dc}^*(t)), \ \omega_{vc} > 0, \ \forall t \geq 0, \tag{6}$$

for a given reference signal of $v_{dc,ref}(t)$. This study investigates the tracking performance improvement by modifying the LPF dynamics of (6) as

$$\dot{v}_{dc}^*(t) = \hat{\omega}_{vc}(t)(v_{dc,ref}(t) - v_{dc}^*(t)), \ \forall t \geq 0, \tag{7}$$

where $\hat{\omega}_{vc}(t)$ denotes the time-varying cut-off frequency associated with the control gain to be designed later. The time-varying LPF of (7) is called the target dynamics in this study. Section 3.1 presents a control algorithm with the classical cascade structure, and Section 3.2 analyzes the closed-loop properties.

3.1. Controller Design

This section develops the DC-link voltage-loop, including an auto-tuner, and the current-loop in a separated manner. To this end, rewrite the DC-link voltage and current dynamics of (1) and (4) with respect to the nominal parameter values of $L_{x,0}$, $x = d, q$, $R_{s,0}$, $\lambda_{PM,0}$, and C_0 as

$$\begin{aligned} C_0\dot{v}_{dc}(t) &= \frac{\omega(t)}{v_{dc}(t)}T_{e,0}(t) + d_v(t) \\ &= \frac{\omega(t)}{v_{dc}(t)}bi_q(t) + \frac{\omega(t)}{v_{dc}(t)}\frac{3}{2}P\Delta L_{dq,0}i_d(t)i_q(t) + d_v(t), \end{aligned} \tag{8}$$

$$\mathbf{L}_{dq,0}\dot{\mathbf{i}}_{dq}(t) = -R_{s,0}\mathbf{i}_{dq}(t) + \mathbf{p}_0(\mathbf{i}_{dq}(t))\omega_r(t) + \mathbf{u}(t) + \mathbf{d}_0(t),\ \forall t \geq 0, \tag{9}$$

where $b := \frac{3}{2}P\lambda_{PM,0}$, $T_{e,0}(t) := T_e(i_d(t), i_q(t))\Big|_{L_x = L_{x,0}, \lambda_{PM} = \lambda_{PM,0}}$, $\mathbf{p}_0(\mathbf{i}_{dq}(t)) := \begin{bmatrix} L_{q,0}i_q(t) & -(L_{d,0}i_d(t) + \lambda_{PM,0}) \end{bmatrix}^T$, and $\mathbf{L}_{dq,0} := \mathrm{diag}\{L_{d,0}, L_{q,0}\}$, $\forall t \geq 0$. The disturbances of $d_v(t)$ and $\mathbf{d}_0(t) := \begin{bmatrix} d_{d,0}(t) & d_{q,0}(t) \end{bmatrix}^T$ represent the model-plant mismatches and load variations.

3.1.1. DC-Link Voltage-Loop

This section handles the q-axis current reference of $i_{q,ref}(t)$ as a design variable. First, consider the DC-link voltage dynamics of (8) as

$$\begin{aligned} C_0\dot{v}_{dc}(t) &= \frac{\omega(t)}{v_{dc}(t)}bi_q(t) + \frac{\omega(t)}{v_{dc}(t)}\frac{3}{2}P\Delta L_{dq,0}i_d(t)i_q(t) + d_v(t) \\ &= \frac{\omega(t)}{v_{dc}(t)}bi_{q,ref}(t) - \frac{\omega(t)}{v_{dc}(t)}b\tilde{i}_q(t) + \frac{\omega(t)}{v_{dc}(t)}\frac{3}{2}\Delta L_{dq,0}i_d(t)i_q(t) + d_v(t),\ \forall t \geq 0, \end{aligned} \tag{10}$$

with $\tilde{i}_q(t) := i_{q,ref}(t) - i_q(t), \forall t \geq 0$. Then, the q-axis current reference is proposed as

$$i_{q,ref}(t) = \frac{v_{dc}(t)}{b\omega(t)}(C_0\hat{\omega}_{vc}(t)\tilde{v}_{dc}(t) - \frac{\omega(t)}{v_{dc}(t)}\frac{3}{2}\Delta L_{dq,0}i_d(t)i_q(t) - \hat{d}_v(t)),\ \forall t \geq 0, \tag{11}$$

where the DC-link voltage tracking error is defined as $\tilde{v}_{dc}(t) := v_{dc,ref}(t) - v_{dc}(t)$, $\forall t \geq 0$, and the variable control gain of $\hat{\omega}_{vc}(t)$ comes from the proposed auto-tuning mechanism:

$$\dot{\hat{\omega}}_{vc}(t) = \gamma_{at}(\tilde{v}_{dc}^2(t) + \rho_{at}\tilde{\omega}_{vc}(t)),\ \gamma_{at} > 0,\ \rho_{at} > 0\ \forall t \geq 0, \tag{12}$$

with $\tilde{\omega}_{vc}(t) := \omega_{vc} - \hat{\omega}_{vc}(t)$, $\hat{\omega}_{vc}(0) = \omega_{vc} > 0$, $\forall t \geq 0$. The dynamical compensator of $\hat{d}_v(t)$ is updated as

$$\dot{z}_v(t) = -l_v z_v(t) - l_v^2 C_0 v_{dc}(t) - l_v T_{e,0}(t)\frac{\omega(t)}{v_{dc}(t)}, \tag{13}$$

$$\hat{d}_v(t) = z_v(t) + l_v C_0 v_{dc}(t),\ l_v > 0,\ \forall t \geq 0, \tag{14}$$

with $z_v(t)$ being the state-variable, which is the DOB for the DC-link voltage loop. It is easy to see that the proposed DC-link voltage loop controller produces the closed-loop dynamics by substituting (11) in (10) as

$$\begin{aligned}\dot{v}_{dc}(t) &= \hat{\omega}_{vc}(t)\tilde{v}_{dc}(t) - \frac{\omega(t)}{C_0 v_{dc}(t)} b\tilde{i}_q(t) + \frac{1}{C_0}\tilde{d}_v(t) \\ &= \omega_{vc}\tilde{v}_{dc}(t) - \tilde{\omega}_{vc}(t)\tilde{v}_{dc}(t) - \frac{\omega(t)}{C_0 v_{dc}(t)} b\tilde{i}_q(t) + \frac{1}{C_0}\tilde{d}_v(t),\ \forall t \geq 0, \end{aligned} \tag{15}$$

with $\tilde{d}_v(t) := d_v(t) - \hat{d}_v(t), \forall t \geq 0$.

Remark 1. *Unlike [20], the voltage-loop controller of (11) feedbacks the tracking error with the time-varying gain of $C_0\hat{\omega}_{vc}(t)$ and the proposed auto-tuning mechanism of (12) updates the cut-off frequency of $\hat{\omega}_{vc}(t)$. Moreover, the resulting closed-loop behavior is also analyzed in Section 3.2 in a different way.* ♢

3.1.2. Current-Loop

Defining the current error of $\tilde{\mathbf{i}}_{dq}(t) := \mathbf{i}_{dq,ref}(t) - \mathbf{i}_{dq}(t)$ with the current reference of $\mathbf{i}_{dq,ref}(t) := \begin{bmatrix} i_{d,ref}(t) & i_{q,ref}(t) \end{bmatrix}^T$, it follows from (9) that

$$\begin{aligned}\mathbf{L}_{dq,0}\dot{\tilde{\mathbf{i}}}_{dq}(t) &= \mathbf{L}_{dq,0}\dot{\mathbf{i}}_{dq,ref}(t) - \mathbf{L}_{dq,0}\dot{\mathbf{i}}_{dq}(t) \\ &= R_{s,0}\mathbf{i}_{dq}(t) - \mathbf{p}_0(\mathbf{i}_{dq}(t))\omega_r(t) - \mathbf{u}(t) + \mathbf{d}(t),\ \forall t \geq 0, \end{aligned} \tag{16}$$

with $\mathbf{d}(t) := \mathbf{L}_{dq,0}\dot{\mathbf{i}}_{dq,ref}(t) - \mathbf{d}_0(t), \forall t \geq 0$. A controller is suggested to stabilize the error dynamics of (16) as follows:

$$\mathbf{u}(t) = R_{s,0}\mathbf{i}_{dq}(t) - \mathbf{p}_0(\mathbf{i}_{dq}(t))\omega_r(t) + \hat{\mathbf{d}}(t) + \mathbf{L}_{dq,0}\omega_{cc}\tilde{\mathbf{i}}_{dq}(t),\ \omega_{cc} > 0,\ \forall t \geq 0, \tag{17}$$

with the dynamical compensator of $\hat{\mathbf{d}}(t)$ updating as

$$\dot{\mathbf{z}}(t) = -l\mathbf{z}(t) - l^2\mathbf{L}_{dq,0}\tilde{\mathbf{i}}_{dq}(t) + l(-R_{s,0}\mathbf{i}_{dq}(t) + \mathbf{p}_0(\mathbf{i}_{dq}(t))\omega_r(t) + \mathbf{u}(t)), \tag{18}$$

$$\hat{\mathbf{d}}(t) = \mathbf{z}(t) + l\mathbf{L}_{dq,0}\tilde{\mathbf{i}}_{dq}(t),\ l > 0,\ \forall t \geq 0, \tag{19}$$

using the state-variable of $\mathbf{z}(t)$, which is called the DOB for the current-loop. It is also easy to see that the proposed controller of (17) produces closed-loop current error dynamics by combining (16) and (17) as

$$\dot{\tilde{\mathbf{i}}}_{dq}(t) = -\omega_{cc}\tilde{\mathbf{i}}_{dq}(t) + \mathbf{L}_{dq}^{-1}\tilde{\mathbf{d}}(t),\ \forall t \geq 0, \tag{20}$$

with $\tilde{\mathbf{d}}(t) := \mathbf{d}(t) - \hat{\mathbf{d}}(t), \forall t \geq 0$.

3.2. Closed-Loop Properties

This section presents the useful properties of the closed-loop system and shows that the closed-loop system guarantees the control objective of (5) by analyzing the closed-loop system behaviors. Firstly, Theorem 1 provides the convergence property.

Theorem 1. *The closed-loop system controlled by the proposed control law of (11)–(14), (17)–(19) gives the output voltage convergence property. i.e.,*

$$\lim_{t\to\infty} v_{dc}(t) = v_{dc,ref}(t) \tag{21}$$

as $\dot{v}_{dc,ref}(t), \dot{d}_v(t) \to 0$ and $\dot{\boldsymbol{d}}(t) \to \boldsymbol{0}$, exponentially. ♢

Proof. First, rewrite the DOBs for the DC-link voltage- and current-loops of (13), (14), (18), and (19) as

$$\begin{aligned}\dot{\hat{d}}_v - l_v C_0 \dot{v}_{dc} &= -l_v(\hat{d}_v - l_v C_0 v_{dc}) - l_v^2 C_0 v_{dc} - l_v T_{e,0}\frac{\omega}{v_{dc}},\\ \dot{\hat{\mathbf{d}}} - l\mathbf{L}_{dq,0}\dot{\tilde{\mathbf{i}}}_{dq} &= -l(\hat{\mathbf{d}} - l\mathbf{L}_{dq,0}\tilde{\mathbf{i}}_{dq}) - l^2\mathbf{L}_{dq,0}\tilde{\mathbf{i}}_{dq} + l(-R_{s,0}\mathbf{i}_{dq} + \mathbf{p}_0\omega_r + \mathbf{u}),\ \forall t \geq 0,\end{aligned}$$

which gives their error dynamics (by (8) and (16)):

$$\dot{\tilde{d}}_v = -l_v\tilde{d}_v + \dot{d}_v,\ \dot{\tilde{\mathbf{d}}} = -l\tilde{\mathbf{d}} + \dot{\mathbf{d}},\ \forall t \geq 0. \tag{22}$$

Defining the DC-link voltage error of $\tilde{v}_{dc}(t) := v_{dc,ref}(t) - v_{dc}(t)$, $\forall t \geq 0$, it follows from (15) that

$$\begin{aligned}\dot{\tilde{v}}_{dc} &= \dot{v}_{dc,ref} - \dot{v}_{dc}\\ &= -\omega_{vc}\tilde{v}_{dc} + \tilde{\omega}_{vc}\tilde{v}_{dc} + \frac{\omega}{C_0 v_{dc}} b\mathbf{e}_2^T\tilde{\mathbf{i}}_{dq} - \frac{1}{C_0}\tilde{d}_v + \dot{v}_{dc,ref},\ \forall t \geq 0,\end{aligned} \tag{23}$$

with $\mathbf{e}_2 := \begin{bmatrix} 0 & 1 \end{bmatrix}^T$. Then, the time-derivative along (12), (20), (22), and (23) of the positive definite function defined as

$$V := \frac{1}{2}\tilde{v}_{dc}^2 + \frac{\kappa_1}{2}\|\tilde{\mathbf{i}}_{dq}\|^2 + \frac{1}{2\gamma_{at}}\tilde{\omega}_{vc}^2 + \frac{\kappa_2}{2}\tilde{d}_v^2 + \frac{\kappa_3}{2}\|\tilde{\mathbf{d}}\|^2,\ \kappa_i > 0,\ i = 1,2,3,\ \forall t \geq 0, \tag{24}$$

is obtained as

$$\begin{aligned}\dot{V} &= \tilde{v}_{dc}\dot{\tilde{v}}_{dc} + \kappa_1\tilde{\mathbf{i}}_{dq}^T\dot{\tilde{\mathbf{i}}}_{dq} - \frac{1}{\gamma_{at}}\tilde{\omega}_{vc}\dot{\tilde{\omega}}_{vc} + \kappa_2\tilde{d}_v\dot{\tilde{d}}_v + \kappa_3\tilde{\mathbf{d}}^T\dot{\tilde{\mathbf{d}}}\\ &= \tilde{v}_{dc}(-\omega_{vc}\tilde{v}_{dc} + \tilde{\omega}_{vc}\tilde{v}_{dc} + \frac{\omega}{C_0 v_{dc}} b\mathbf{e}_2^T\tilde{\mathbf{i}}_{dq} - \frac{1}{C_0}\tilde{d}_v + \dot{v}_{dc,ref})\\ &\quad +\kappa_1\tilde{\mathbf{i}}_{dq}^T(-\omega_{cc}\tilde{\mathbf{i}}_{dq} + \mathbf{L}_{dq}^{-1}\tilde{\mathbf{d}}) - \tilde{\omega}_{vc}(\tilde{v}_{dc}^2 + \rho_{at}\tilde{\omega}_{vc})\\ &\quad -\kappa_2 l_v\tilde{d}_v^2 + \kappa_2\dot{d}_v\tilde{d}_v - \kappa_3 l\|\tilde{\mathbf{d}}\|^2 + \kappa_3\dot{\mathbf{d}}^T\tilde{\mathbf{d}}\\ &= -\omega_{vc}\tilde{v}_{dc}^2 - \kappa_1\omega_{cc}\|\tilde{\mathbf{i}}_{dq}\|^2 - \rho_{at}\tilde{\omega}_{vc}^2 - \kappa_2 l_v\tilde{d}_v^2 - \kappa_3 l\|\tilde{\mathbf{d}}\|^2\\ &\quad +\tilde{v}_{dc}\frac{\omega}{C_0 v_{dc}} b\mathbf{e}_2^T\tilde{\mathbf{i}}_{dq} - \frac{1}{C_0}\tilde{v}_{dc}\tilde{d}_v + \kappa_1\tilde{\mathbf{i}}_{dq}^T\mathbf{L}_{dq}^{-1}\tilde{\mathbf{d}} + \mathbf{w}^T\mathbf{y},\ \forall t \geq 0,\end{aligned}$$

where $\mathbf{w} := \begin{bmatrix} \dot{v}_{dc,ref} & \kappa_2\dot{d}_v & \kappa_3\dot{\mathbf{d}}^T \end{bmatrix}^T$ and $\mathbf{y} := \begin{bmatrix} \tilde{v}_{dc} & \tilde{d}_v & \tilde{\mathbf{d}}^T \end{bmatrix}^T$. Applying the Young's inequality of $\mathbf{x}^T\mathbf{y} \leq \frac{\epsilon}{2}\|\mathbf{x}\|^2 + \frac{1}{2\epsilon}\|\mathbf{y}\|^2$, $\forall \epsilon > 0$, $\forall \mathbf{x}, \mathbf{y} \in \mathbb{R}^n$ to the indefinite terms of $\dot{V}$, it holds that

$$\begin{aligned}\dot{V} &\leq -\frac{\omega_{vc}}{3}\tilde{v}_{dc}^2 - (\kappa_1\omega_{cc} - \frac{\omega_{max}^2 b^2}{4\omega_{vc}C_0^2 v_{dc,min}^2} - \frac{1}{2})\|\tilde{\mathbf{i}}_{dq}\|^2 - \rho_{at}\tilde{\omega}_{vc}^2\\ &\quad -(\kappa_2 l_v - \frac{1}{4\omega_{vc}C_0^2})\tilde{d}_v^2 - (\kappa_3 l - \frac{\kappa_1^2\|\mathbf{L}_{dq}^{-1}\|^2}{2})\|\tilde{\mathbf{d}}\|^2 + \mathbf{w}^T\mathbf{y},\ \forall t \geq 0,\end{aligned}$$

with ω_{max} and $v_{dc,min}$ being the maximum and minimum values of ω and v_{dc}, respectively, whose upper bound can be obtained by the constants of $\kappa_1 := \frac{1}{\omega_{cc}}(\frac{\omega_{max}^2 b^2}{4\omega_{vc}C_0^2 v_{dc,min}^2} + 1)$, $\kappa_2 := \frac{1}{l_v}(\frac{1}{4\omega_{vc}C_0^2} + \frac{1}{2})$, and $\kappa_3 := \frac{1}{l}(\frac{\kappa_1^2\|\mathbf{L}_{dq}^{-1}\|^2}{2} + \frac{1}{2})$ as

$$\begin{aligned}\dot{V} &\leq -\frac{\omega_{vc}}{3}\tilde{v}_{dc}^2 - \frac{1}{2}\|\tilde{\mathbf{i}}_{dq}\|^2 - \rho_{at}\tilde{\omega}_{vc}^2 - \frac{1}{2}\tilde{d}_v^2 - \frac{1}{2}\|\tilde{\mathbf{d}}\|^2 + \mathbf{w}^T\mathbf{y}\\ &\leq -\alpha V + \mathbf{w}^T\mathbf{y},\ \forall t \geq 0,\end{aligned} \tag{25}$$

with $\alpha := \min\{\frac{2\omega_{vc}}{3}, \frac{1}{\kappa_1}, 2\rho_{at}\gamma_{at}, \frac{1}{\kappa_2}, \frac{1}{\kappa_3}\}$, which completes the proof. □

Lemma 1 presents the boundedness property of the auto-tuning algorithm of (12), which simplifies the proof of performance recovery property of Theorem 2.

Lemma 1. *The variable cut-off frequency of $\hat{\omega}_{vc}(t)$ coming from the auto-tuner of (12) satisfies*

$$\hat{\omega}_{vc}(t) \geq \omega_{vc}, \forall t \geq 0. \tag{26}$$

◊

Proof. The auto-tuner update rule of (12) is equivalent to the expression of

$$\dot{\hat{\omega}}_{vc} = -\gamma_{at}\rho_{at}\hat{\omega}_{vc} + \gamma_{at}\rho_{at}\omega_{vc} + \gamma_{at}\tilde{v}_{dc}^2,$$

which indicates that (by integrating both sides)

$$\begin{aligned}
\hat{\omega}_{vc} &= e^{-\gamma_{at}\rho_{at}t}\omega_{vc} + \int_0^t e^{-\gamma_{at}\rho_{at}(t-\tau)}(\gamma_{at}\rho_{at}\omega_{vc} + \gamma_{at}\tilde{v}_{dc}^2)d\tau \\
&\geq e^{-\gamma_{at}\rho_{at}t}\omega_{vc} + \gamma_{at}\rho_{at}\omega_{vc}e^{-\gamma_{at}\rho_{at}t}\int_0^t e^{\gamma_{at}\rho_{at}\tau}d\tau \\
&= \omega_{vc}, \ \forall t \geq 0.
\end{aligned}$$

□

Theorem 2 asserts that the proposed controller establishes the control objective of (5), that is the performance recovery property, using the result of Lemma 1.

Theorem 2. *The closed-loop system controlled by the proposed control law of (11)–(14), (17)–(19) ensures the performance recovery property. i.e.,*

$$\lim_{t\to\infty} v_{dc}(t) = v_{dc}^*(t) \tag{27}$$

as $\dot{d}_v(t) \to 0$ and $\dot{\boldsymbol{d}}(t) \to \boldsymbol{0}$, exponentially. ◊

Proof. Using (7) and (15), the dynamics of the tracking error $\tilde{v}_{dc}^* := v_{dc}^* - v_{dc}$ is obtained as

$$\dot{\tilde{v}}_{dc}^* = -\hat{\omega}_{vc}\tilde{v}_{dc}^* + \frac{\omega}{C_0 v_{dc}} b\mathbf{e}_2^T\tilde{\mathbf{i}}_{dq} - \frac{1}{C_0}\tilde{d}_v, \ \forall t \geq 0, \tag{28}$$

with $\mathbf{e}_2 = \begin{bmatrix} 0 & 1 \end{bmatrix}^T$. The time-derivative along (20), (22), and (28) of the positive definite function given by

$$V^* := \frac{1}{2}(\tilde{v}_{dc}^*)^2 + \frac{c_1}{2}\|\tilde{\mathbf{i}}_{dq}\|^2 + \frac{c_2}{2}\tilde{d}_v^2 + \frac{c_3}{2}\|\tilde{\mathbf{d}}\|^2, \ c_i > 0, \ i = 1,2,3, \ \forall t \geq 0, \tag{29}$$

is given by

$$\begin{aligned}
\dot{V}^* &= \tilde{v}_{dc}^*(-\hat{\omega}_{vc}\tilde{v}_{dc}^* + \frac{\omega}{C_0 v_{dc}} b\mathbf{e}_2^T\tilde{\mathbf{i}}_{dq} - \frac{1}{C_0}\tilde{d}_v) \\
&\quad + c_1\tilde{\mathbf{i}}_{dq}^T(-\omega_{cc}\tilde{\mathbf{i}}_{dq} + \mathbf{L}_{dq}^{-1}\tilde{\mathbf{d}}) - c_2 l_v\tilde{d}_v^2 - c_3 l\|\tilde{\mathbf{d}}\|^2 + c_2 l_v\dot{d}_v\tilde{d}_v + c_3 l\dot{\mathbf{d}}^T\tilde{\mathbf{d}} \\
&= -\hat{\omega}_{vc}(\tilde{v}_{dc}^*)^2 - c_1\omega_{cc}\|\tilde{\mathbf{i}}_{dq}\|^2 - c_2 l_v\tilde{d}_v^2 - c_3 l\|\tilde{\mathbf{d}}\|^2 \\
&\quad + \tilde{v}_{dc}^*\frac{\omega}{C_0 v_{dc}} b\mathbf{e}_2^T\tilde{\mathbf{i}}_{dq} - \tilde{v}_{dc}^*\frac{1}{C_0}\tilde{d}_v + c_1\tilde{\mathbf{i}}_{dq}^T\mathbf{L}_{dq}^{-1}\tilde{\mathbf{d}} + c_2 l_v\dot{d}_v\tilde{d}_v + c_3 l\dot{\mathbf{d}}^T\tilde{\mathbf{d}}, \ \forall t \geq 0.
\end{aligned}$$

Applying the result of Lemma 1 and the Young's inequality to the indefinite terms of $\dot{V}^*$, it holds that

$$\begin{aligned}\dot{V}^* \leq & -\frac{\omega_{vc}}{3}(\tilde{v}_{dc}^*)^2 - (c_1\omega_{cc} - \frac{\omega_{max}^2 b^2}{4\omega_{vc}C_0^2 v_{dc,min}^2} - \frac{1}{2})\|\tilde{\mathbf{i}}_{dq}\|^2 \\ & -(c_2 l_v - \frac{3}{4\omega_{vc}C_0^2})\tilde{d}_v^2 - (c_3 l - \frac{c_1^2\|\mathbf{L}_{dq}^{-1}\|^2}{2})\|\tilde{\mathbf{d}}\|^2 + c_2 l_v \dot{d}_v \tilde{d}_v + c_3 l \dot{\mathbf{d}}^T\tilde{\mathbf{d}},\ \forall t \geq 0,\end{aligned}$$

whose upper bound can be obtained by the constants of $c_1 := \frac{1}{\omega_{cc}}(\frac{\omega_{max}^2 b^2}{4\omega_{vc}C_0^2 v_{dc,min}^2} + 1)$, $c_2 := \frac{1}{l_v}(\frac{1}{4\omega_{vc}C_0^2} + \frac{1}{2})$, and $c_3 := \frac{1}{l}(\frac{c_1^2\|\mathbf{L}_{dq}^{-1}\|^2}{2} + \frac{1}{2})$ as

$$\begin{aligned}\dot{V}^* &\leq -\frac{\omega_{vc}}{3}(\tilde{v}_{dc}^*)^2 - \frac{1}{2}\|\tilde{\mathbf{i}}_{dq}\|^2 - \frac{1}{2}\tilde{d}_v^2 - \frac{1}{2}\|\tilde{\mathbf{d}}\|^2 + c_2 l_v \dot{d}_v \tilde{d}_v + c_3 l \dot{\mathbf{d}}^T\tilde{\mathbf{d}} \\ &\leq -\alpha^* V^* + c_2 l_v \dot{d}_v \tilde{d}_v + c_3 l \dot{\mathbf{d}}^T\tilde{\mathbf{d}},\ \forall t \geq 0, \end{aligned} \tag{30}$$

with $\alpha^* := \min\{\frac{2\omega_{vc}}{3}, \frac{1}{c_1}, \frac{1}{c_2}, \frac{1}{c_3}\}$, which completes the proof. □

It is not obvious for the proposed controller to ensure the offset-free property in actual implementations due to the absence of integral actions of tracking errors in the controller law of (17) and (11). Theorem 3 addresses this issue.

Theorem 3. *The control system controlled by the proposed control law of (11)–(14), (17)–(19) establishes the tracking objective of (5) without offset-errors. i.e.,*

$$v_{dc}(\infty) = v_{dc,ref}(\infty), \tag{31}$$

where $lim_{t\to\infty} v_{dc}(t) = v_{dc}(\infty)$ *and* $\lim_{t\to\infty} v_{dc,ref}(t) = v_{dc,ref}(\infty)$. ◊

Proof. The closed-loop dynamics of (15), (20), and (22) give the steady-state equations as

$$0 = \hat{\omega}_{vc}(\infty)\tilde{v}_{dc}(\infty) - \frac{\omega(\infty)}{C_0 v_{dc}(\infty)} b\mathbf{e}_2^T\tilde{\mathbf{i}}_{dq}(\infty) + \frac{1}{C_0}\tilde{d}_v(\infty), \tag{32}$$

$$\mathbf{0} = -\omega_{cc}\tilde{\mathbf{i}}_{dq}(\infty) + \mathbf{L}_{dq}^{-1}\tilde{\mathbf{d}}(\infty), \tag{33}$$

$$0 = \tilde{d}_v(\infty),\ \mathbf{0} = \tilde{\mathbf{d}}(\infty). \tag{34}$$

The equation of (33) implies $\tilde{\mathbf{i}}_{dq}(\infty) = \mathbf{0}$ from the equation of (34), which shows that $\tilde{v}_{dc}(\infty) = 0$ by the combination of (32) and (34). Therefore, the proposed controller removes the offset errors as long as the closed-loop system reaches a steady-state. □

4. Simulations

In this section, numerical verifications were carried out to demonstrate the effectiveness of the proposed scheme, and the FL controller is used for comparison. A wind power system driven by a PMSG was emulated by using the function blocks provided in the PSIM software. The control algorithms were built by C-language, which results in the DLL block. The control output signals of $u_x(t)$, $x = d, q$, were synthesized using the three-phase inverter with the pulse-wide modulation (PWM). The control and PWM periods were selected as 0.1 ms. The system parameters were chosen as

$$\begin{aligned} R_s &= 0.099\ \Omega,\ L_x = 4.07\ mH,\ x = d, q,\ \lambda_{PM} = 0.3166\ Wb,\ P = 40, \\ J &= 0.02\ kgm^2,\ B = 0.000425\ Nm/rad/s,\ C = 2350\ \mu F, \end{aligned} \tag{35}$$

and the control algorithms were constructed using the nominal system parameters:

$$R_{s,0} = 0.7R_s,\ L_{x,0} = 1.5L_x,\ \lambda_{PM,0} = 1.2\lambda_{PM},\ C_0 = 0.6C,\ x = d, q, \tag{36}$$

instead of the use of true system parameters to consider the model-plant mismatches. The wind turbine parameters were set as follows; nominal output power: 15 kW, inertia: 1.5×10^{-3} kgm^2, base rotational speed: 55 rpm, and initial rotational speed: 15 rpm. The wind pattern was emulated using the wind model based-on Weibull distribution [27]. The structure of the implemented wind power system is shown in Figure 2.

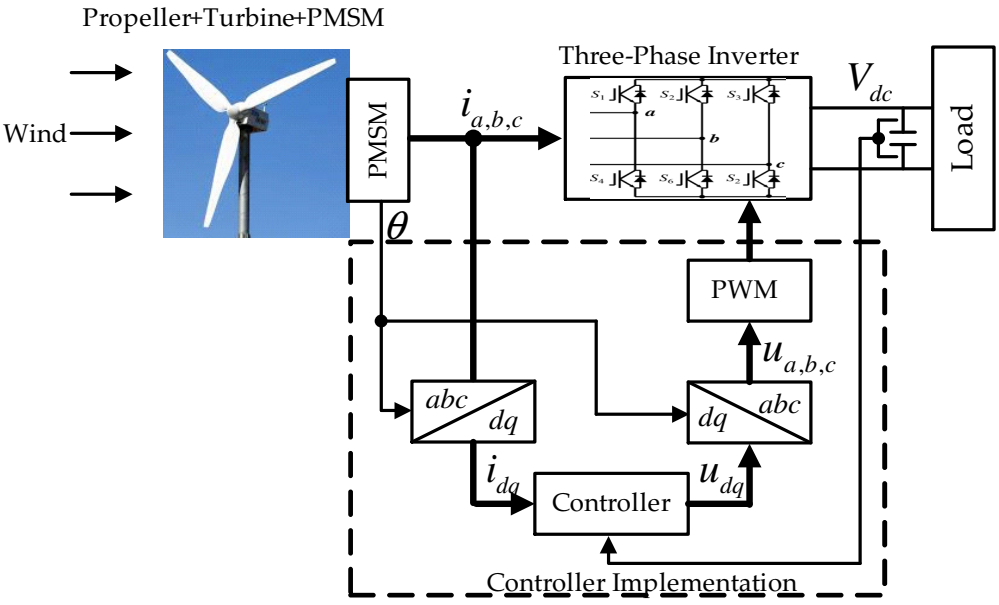

Figure 2. Closed-loop system implementation.

The control law of FL method is described as

$$u_d(t) = L_{d,0}\omega_{cc}\tilde{i}_d(t) + R_{s,0}\omega_{cc}\int_0^t \tilde{i}_d(\tau)d\tau - L_{q,0}\omega_r(t)i_q(t), \tag{37}$$

$$u_q(t) = L_{q,0}\omega_{cc}\tilde{i}_q(t) + R_{s,0}\omega_{cc}\int_0^t \tilde{i}_q(\tau)d\tau + L_{d,0}\omega_r(t)i_d(t) + \lambda_{PM,0}\omega_r(t),\ \forall t \geq 0, \tag{38}$$

with

$$i_{q,ref}(t) = \frac{v_{dc}(t)}{b\omega(t)}\left(2C_0\omega_{vc}\tilde{v}_{dc}(t) + C_0\omega_{vc}^2\int_0^t \tilde{v}_{dc}(\tau)d\tau\right),\ \forall t \geq 0, \tag{39}$$

where $\tilde{v}_{dc}(t) = v_{dc,ref}(t) - v_{dc}(t), \forall t \geq 0$, which gives the closed-loop transfer functions for the voltage- and current-loops:

$$\frac{I_x(s)}{I_{x,ref}(s)} = \frac{\mathcal{L}\{i_x(t)\}}{\mathcal{L}\{i_{x,ref}(t)\}} = \frac{\omega_{cc}}{s+\omega_{cc}},\ x = d, q,$$

$$\frac{V_{dc}(s)}{V_{dc,ref}(s)} = \frac{\mathcal{L}\{v_{dc}(t)\}}{\mathcal{L}\{v_{dc,ref}(t)\}} = \frac{\omega_{vc}}{s+\omega_{vc}},$$

approximately, via pole-zero cancellation in the absence of model-plant mismatches, where $\mathcal{L}(\cdot)$ denotes the Laplace transform operator. The design parameters commonly used for the two controllers were set to $f_{cc} = 200$ Hz and $f_{vc} = 4$ Hz for $\omega_{cc} = 2\pi f_{cc} = 1256$ rad/s and $\omega_{vc} = 2\pi f_{vc} = 25.1$ rad/s.

The proposed controller was tuned as $l_v = l = 50$, $\gamma_{at} = 0.05$, and $\rho_{at} = 15/\gamma_{at}$. Note that the d-axis current reference was set to zero for simplicity.

The first verification was carried out to demonstrate the robustness improvement for several loads under the voltage tracking control mode. The DC-link voltage reference was given in the form of a pulse from 300 V to 500 V, and the closed-loop tracking behavior changes were observed for three resistive loads, $R_L = 30, 60, 120\ \Omega$. Figure 3 shows the comparison results of the DC-link voltage response, which implies that the proposed controller effectively improves the closed-loop robustness by preventing closed-loop performance variation in spite of load changes. From Figure 4, it can be seen that the proposed controller drives the q-axis current more rapidly than the FL controller, resulting in better closed-loop robustness. The corresponding cut-off frequency and DOB behaviors are presented in Figure 5, and Figure 6 shows the wind velocity pattern from the Weibull distribution.

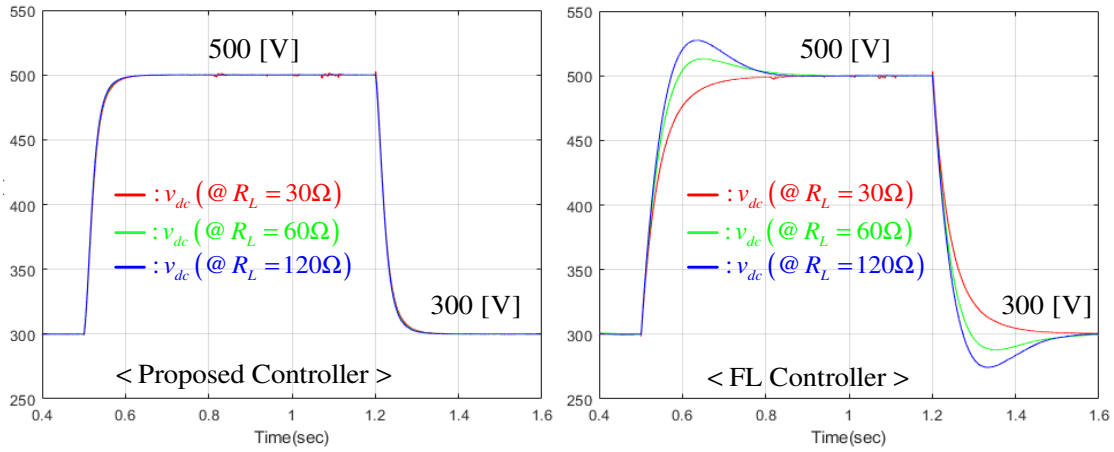

Figure 3. DC-link voltage tracking behavior changes for three loads, $R_L = 30, 60, 120\ \Omega$.

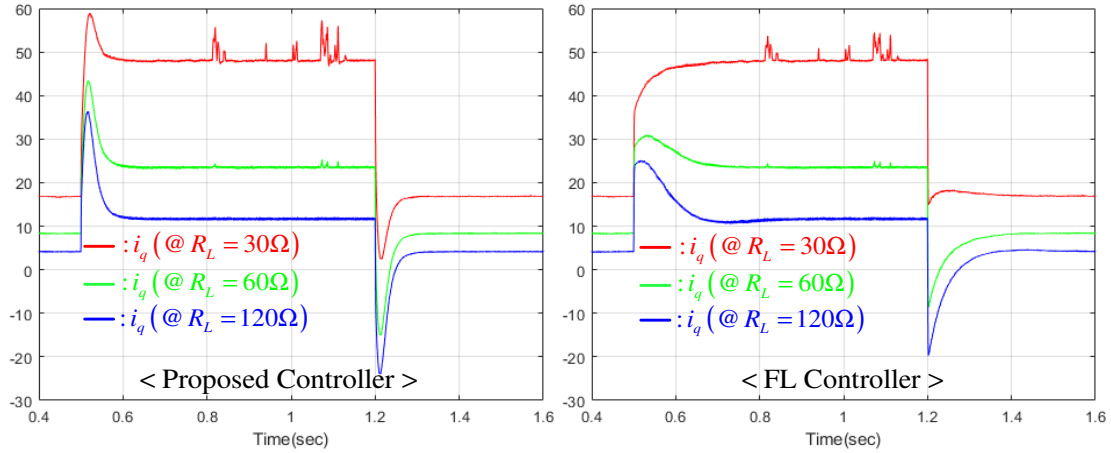

Figure 4. q-axis current response comparison result under DC-link voltage tracking control mode.

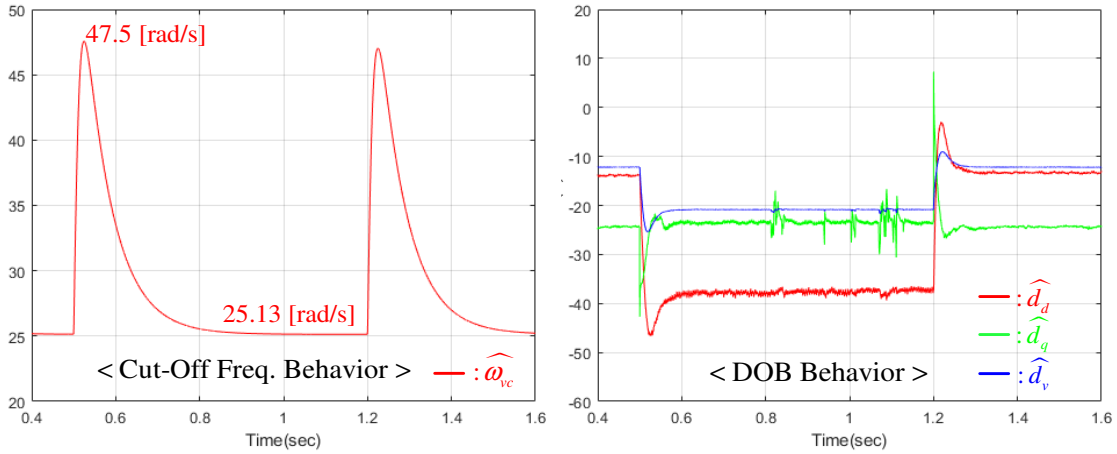

Figure 5. Cut-off frequency and DOB responses of proposed controller under DC-link voltage tracking control mode.

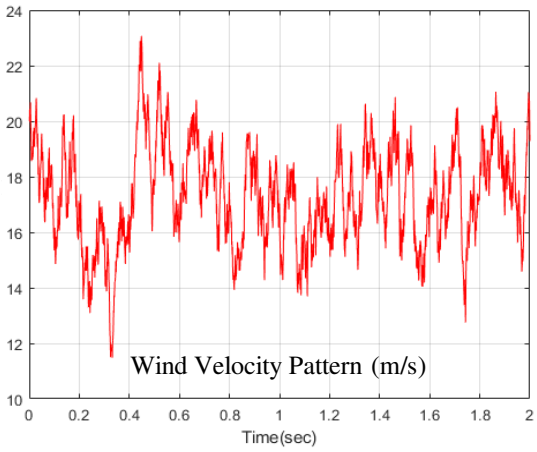

Figure 6. Wind velocity pattern from Weibull distribution.

The second verification was carried out to observe the closed-loop robustness under the voltage regulation mode with several sudden load change scenarios. The DC-link voltage reference was fixed to 300 V, and the closed-loop regulation behavior changes were observed for three resistive load change scenarios: (a) restoring the resistive load after increasing it from $R_L = 60\ \Omega$ to $R_L = 24\ \Omega$; (b) restoring the resistive load after increasing it from $R_L = 120\ \Omega$ to $R_L = 30\ \Omega$; and (c) restoring the resistive load after increasing it from $R_L = 30\ \Omega$ to $R_L = 17\ \Omega$. Figure 7, which shows the comparison result of the closed-loop DC-link voltage response, indicates that the closed-loop robustness improvement is achieved by the proposed technique, as it decreases the overshoots/undershoots considerably. The corresponding q-axis current response is given in Figure 8, which indicates that the proposed controller leads to a rapid current dynamics for a better DC-link voltage regulation performance.

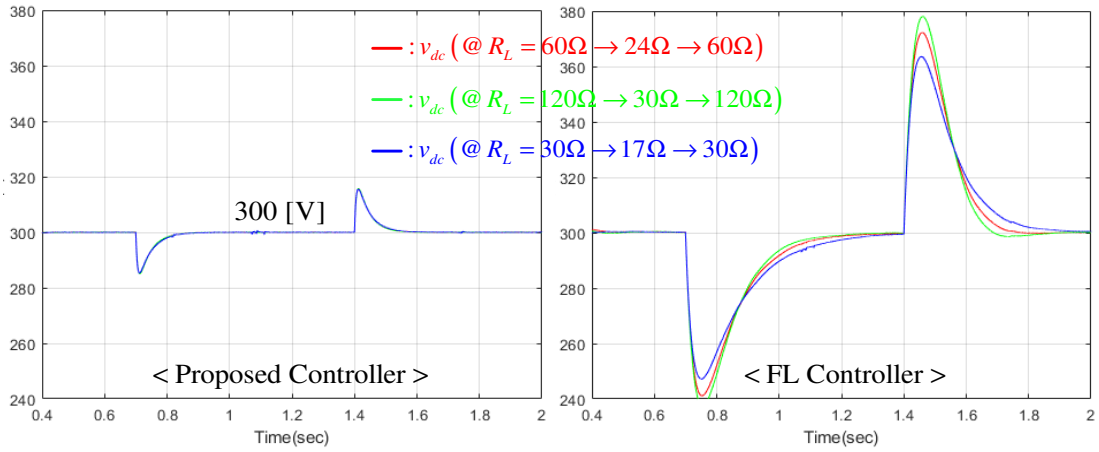

Figure 7. DC-link voltage regulation behavior changes under three resistive load change scenarios: (**a**) $R_L = 60\ \Omega \rightarrow 24\ \Omega \rightarrow 60\ \Omega$; (**b**) $R_L = 120\ \Omega \rightarrow 30\ \Omega \rightarrow 120\ \Omega$; and (**c**) $R_L = 30\ \Omega \rightarrow 17\ \Omega \rightarrow 30\ \Omega$.

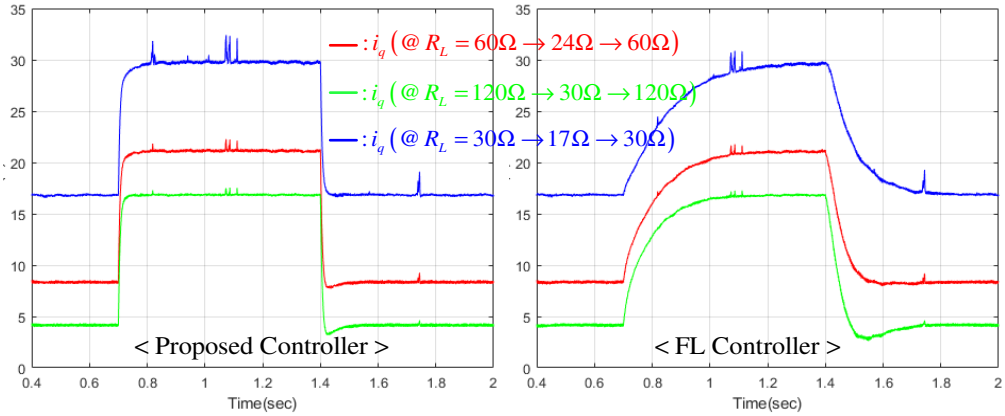

Figure 8. q-axis current response comparison under DC-link voltage regulation mode.

The third verification shows the output voltage tracking performance improvement at the resistive load $R_L = 60\ \Omega$, compared with a recent DOB-based technique introduced in [20], which is given by

$$u_d(t) = R_{s,0} i_d(t) - L_{q,0}\omega_r(t) i_q(t) + L_{d,0}\lambda_{cc}\tilde{i}_d(t) + \hat{d}_d(t), \tag{40}$$

$$u_q(t) = R_{s,0} i_q(t) + L_{d,0}\omega_r(t) i_d(t) + \lambda_{PM,0}\omega_r(t) + \frac{L_{q,0}\omega(t)}{C_0 v_{dc}(t)} b\tilde{v}_{dc}^* + L_{q,0}\lambda_{cc}\tilde{i}_q(t) + \hat{d}_q(t),\ \lambda_{cc} > 0,\ \forall t \geq 0, \tag{41}$$

with the DOBs of

$$\hat{d}_x(t) = \zeta_x(t) + l_x L_{x,0}\tilde{i}_x(t),\ x = d, q,$$

$$\dot{\zeta}_d(t) = -l_d\zeta_d(t) - l_d^2 L_{d,0}\tilde{i}_d(t) + l_d\Big(- R_{s,0} i_d(t) + L_{q,0}\omega_r(t) i_q(t) + u_d(t)\Big),\ l_d > 0, \tag{42}$$

$$\dot{\zeta}_q(t) = -l_q\zeta_q(t) - l_q^2 L_{q,0}\tilde{i}_q(t) + l_q\Big(- R_{s,0} i_q(t) - L_{d,0}\omega_r(t) i_d(t) - \lambda_{PM,0}\omega_r(t) + u_q(t)\Big), l_q > 0,\ \forall t \geq 0. \tag{43}$$

The corresponding q-axis current reference is updated as

$$i_{q,ref}(t) = \frac{v_{dc}(t)}{b\omega(t)}\left(C_0\lambda_{vc}\tilde{v}_{dc}^*(t) - \frac{\omega(t)}{v_{dc}(t)}\frac{3}{2}P\Delta L_{dq,0} i_d(t) i_q(t) + \hat{d}_v(t)\right),\ \lambda_{vc} > 0,\ \forall t \geq 0, \tag{44}$$

along with the output voltage tracking error of $\tilde{v}^*_{dc}(t) = v^*_{dc}(t) - v_{dc}(t)$ where the desired trajectory of $v^*_{dc}(t)$ comes from

$$\dot{v}^*_{dc}(t) = \omega_{vc}\Big(v_{dc,ref}(t) - v^*_{dc}(t)\Big),\ \forall t \geq 0, \tag{45}$$

and the DOB for (44) is given by

$$\begin{aligned}\hat{d}_v(t) &= \zeta_v(t) + l_v C_0 \tilde{v}^*_{dc}(t),\\ \dot{\zeta}_v(t) &= -l_v\zeta_v(t) - l_v^2 C_0 \tilde{v}^*_{dc}(t) + l_v\frac{\omega(t)}{v_{dc}(t)}\left(bi_q(t) + \frac{3}{2}P\Delta L_{dq,0} i_d(t) i_q(t)\right),\ l_v > 0,\ \forall t \geq 0.\end{aligned}$$

The cut-off frequency of ω_{vc} in (45) was set to the same as the initial cut-off frequency of proposed auto-tuning algorithm. The rest of design parameters were adjusted as $\lambda_{vc} = 125.6$, $\lambda_{cc} = 1256$, $l_v = l_d = l_q = 314$. This stage used the three-kinds of sinusoidal reference signals given as $v_{dc,ref}(t) = 500 + 100\sin(2\pi f t)$ with $f = 3, 6, 12$ Hz. Figure 9 shows the tracking performance comparison results, which clearly observes a frequency response performance improvement thanks to the proposed auto-tuning algorithm.

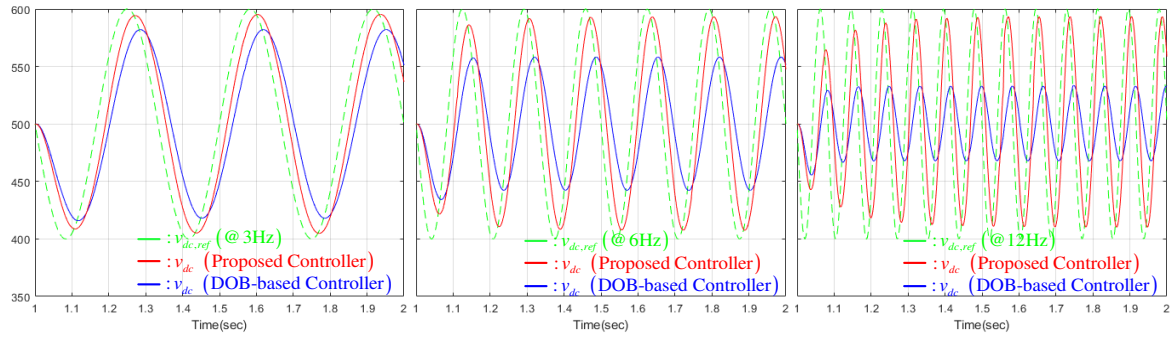

Figure 9. DC-link voltage tracking performance comparison under sinusoidal reference signals at resistive load $R_L = 60\ \Omega$.

In the last verification, the efficacy of the proposed auto-tuner was investigated under the DC-link voltage tracking control mode with a pulse reference from 300 V to 500 V and a resistive load of $R_L = 60\ \Omega$. The initial cut-off frequency was decreased to $f_{vc} = 2$ Hz for $\omega_{cc} = 2\pi f_{vc} = 12.56$ rad/s to demonstrate the effectiveness of the proposed auto-tuner clearly. The resulting DC-link voltage tracking behavior changes are shown in Figure 10, including the variable cut-off frequency dynamics from the auto-tuner. This shows that the proposed auto-tuner effectively boosts the closed-loop tracking performance during transient periods.

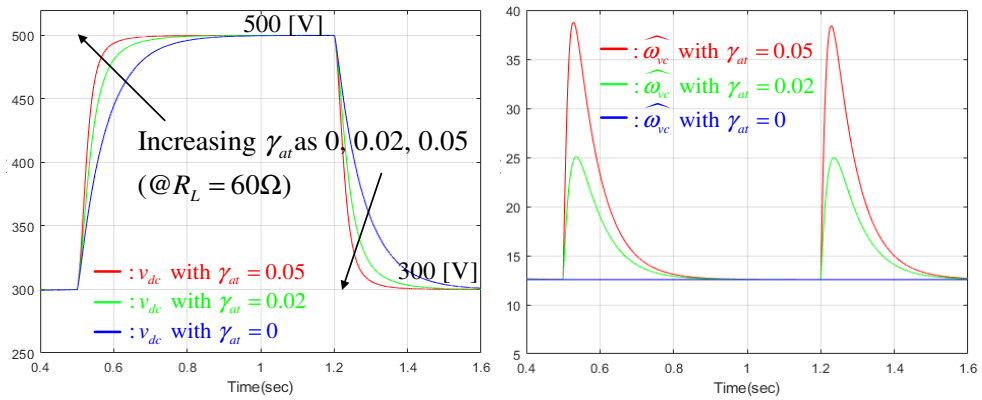

Figure 10. DC-link voltage tracking performance improvement tendency as increasing $\gamma_{at} = 0, 0.02, 0.05$.

From these numerical data, it is seen that the useful closed-loop properties that were proven in Section 3.2 result in practical advantages compared with the FL controller, which depends on the true system parameters. Thus, the proposed controller can be considered as a promising solution for several industrial applications.

5. Conclusions

This study offers a novel DC-link voltage tracking control algorithm with convincing numerical data from realistic simulations. The proposed controller automatically updates the cut-off frequency using the embedded auto-tuning algorithm. Rigorous closed-loop analysis was also presented for the performance recovery and convergence properties. The closed-loop performance improvement was confirmed by simulating a wind power system controlled by the proposed controller. A guideline for systematic and optimal design parameter determination will be provided in a future study with experimental data.

Author Contributions: S.-K.K. surveyed the backgrounds of this research, designed the whole control and estimation algorithms, and performed the simulations so as to show the novelties of the proposed technique. K.-B.L. supervised and financially supported this study.

Funding: This research was supported by a grant (17TLRP-C135446-01,Development of Hybrid Electric Vehicle Conversion Kit for Diesel Delivery Trucks and its Commercialization for Parcel Services) from Transportation & Logistics Research Program (TLRP) funded by Ministry of Land, Infrastructure and Transport of Korean government, and was supported by "Human Resources Program in Energy Technology" of the Korea Institute of Energy Technology Evaluation and Planning (KETEP), granted financial resource from the Ministry of Trade, Industry & Energy, Republic of Korea. (No. 20174030201660)

Conflicts of Interest: The authors declare no conflict of interest.

References

1. Tiwari, R.; Krishnamurthy, K.; Neelakandan, R.B.; Padmanaban, S. Neural Network Based Maximum Power Point Tracking Control with Quadratic Boost Converter for PMSG-Wind Energy Conversion System. *Electronics* **2018**, *7*, 20. [CrossRef]
2. Chen, M.H. Use of Three-Level Power Converters in Wind-Driven Permanent-Magnet Synchronous Generators with Unbalanced Loads. *Electronics* **2015**, *4*, 339–358. [CrossRef]
3. Kamel, T.; Abdelkader, D.; Said, B.; Padmanaban, S.; Iqbal, A. Extended Kalman Filter Based Sliding Mode Control of Parallel-Connected Two Five-Phase PMSM Drive System. *Electronics* **2018**, *7*, 14. [CrossRef]
4. Kim, S.K.; Lee, K.B. Robust Offset-Free Speed Tracking Controller of Permanent Magnet Synchronous Generator for Wind Power Generation Applications. *Electronics* **2018**, *7*, 48. [CrossRef]
5. Asensio, A.P.; Gomez, S.A.; Rodriguez-Amenedo, J.L.; Plaza, M.G.; Carrasco, J.E.G.; de las Morenas, J.M.A.M. A Voltage and Frequency Control Strategy for Stand-Alone Full Converter Wind Energy Conversion Systems. *Energies* **2018**, *11*, 474. [CrossRef]
6. Liu, Z.; Li, K.; Sun, Y.; Wang, J.; Wang, Z.; Sun, K.; Wang, M. A Steady-State Analysis Method for Modular Multilevel Converters Connected to Permanent Magnet Synchronous Generator-Based Wind Energy Conversion Systems. *Energies* **2018**, *11*, 461. [CrossRef]
7. Kim, S.K.; Song, H.; Lee, J. Adaptive Disturbance Observer-Based Parameter-Independent Speed Control of an Uncertain Permanent Magnet Synchronous Machine for Wind Power Generation Applications. *Energies* **2015**, *8*, 4496–4512. [CrossRef]
8. Kazmierkowski, M.P.; Krishnan, R.; Blaabjerg, F. *Control in Power Electronics- Selected Problems*; Academic Press: Cambridge, MA, USA, 2002.
9. Dixon, J.W.; Ooi, B.T. Indirect current control of a unity power factor sinusoidal current boost type three phase rectifier. *IEEE Trans. Ind. Electron.* **1988**, *35*, 508–515. [CrossRef]
10. Matausek, M.R.; Jeftenic, B.I.; Miljkovic, D.M.; Bebic, M.Z. Gain scheduling control of DC motor drive with field weakening. *IEEE Trans. Ind. Electron.* **1996**, *43*, 153–162. [CrossRef]
11. Lee, T.S. Input-output linearization and zero-dynamics control of three-phase AC/DC voltage-source converters. *IEEE Trans. Power Electron.* **2003**, *31*, 11–22.

12. Lee, D.C.; Lee, G.M.; Lee, K.D. DC-bus voltage control of three-phase AC/DC PWM converters using feedback linearization. *IEEE Trans. Ind. Appl.* **2000**, *36*, 826–833.
13. Lee, T.S. Lagrangian Modeling and Passivity Based Control of Three Phase AC to DC Voltage Source Converters. *IEEE Trans. Ind. Electron.* **2004**, *51*, 892–902. [CrossRef]
14. Gomez, M.H.; Ortega, R.; Lagarrigue, F.L.; Escobar, G. Adaptive PI Stabilization of Switched Power Converters. *IEEE. Trans. Control Syst. Technol.* **2010**, *18*, 688–698. [CrossRef]
15. Flores, D.D.P.; Scherpen, J.M.A.; Liserre, M.; de Vries, M.M.J.; Kransse, M.J.; Monopoli, V.G. Passivity-Based Control by Series/Parallel Damping of Single-Phase PWM Voltage Source Converter. *IEEE. Trans. Control Syst. Technol.* **2012**, *3*, 459–471.
16. De Araujo Ribeiro, R.L.; de Oliveira Alves Rocha, T.; de Sousa, R.M.; dos Santos, E.C.; Lima, A.M.N. A Robust DC-Link Voltage Control Strategy to Enhance the Performance of Shunt Active Power Filters Without Harmonic Detection Schemes. *IEEE Trans. Ind. Electron.* **2015**, *62*, 803–813. [CrossRef]
17. Vazquez, S.; Sanchez, J.A.; Carrasco, J.M.; Leon, J.I.; Galvan, E. A model based direct power control for three-phase power converters. *IEEE. Trans. Ind. Electron.* **2008**, *55*, 1647–1657. [CrossRef]
18. Salomonsson, D.; Sannino, A. Direct Power Control Based on Natural Switching Surface for Three-Phase PWM Rectifiers. In Proceedings of the 2007 IEEE 42nd IAS Annual Meeting, Conference Record of the Industry Applications Conference, New Orleans, LA, USA, 23–27 September 2007.
19. Wang, C.; Li, X.; Guo, L.; Li, Y.W. A Nonlinear-Disturbance-Observer-Based DC-Bus Voltage Control for a Hybrid AC/DC Microgrid. *IEEE Trans. Power Electron.* **2014**, *29*, 6162–6177. [CrossRef]
20. Kim, S.K. Proportional-Type Performance Recovery DC-Link Voltage Tracking Algorithm for Permanent Magnet Synchronous Generators. *Energies* **2017**, *10*, 1387. [CrossRef]
21. Rodriguez, J.; Cortes, P. *Predictive Control of Power Converters and Electrical Drives*; Wiley-IEEE Press: Hoboken, NJ, USA, 2012.
22. Bouafia, A.; Gaubert, J.P.; Krim, F. Predictive Direct Power Control of Three-Phase Pulsewidth Modulation (PWM) Rectifier Using Space-Vector Modulation (SVM). *IEEE Trans. Power Electron.* **2010**, *25*, 228–236. [CrossRef]
23. Gan, C.; Wu, J.; Hu, Y.; Yang, S.; Cao, W.; Kirtley, J.L. Online Sensorless Position Estimation for Switched Reluctance Motors Using One Current Sensor. *IEEE Trans. Power Electron.* **2016**, *31*, 7248–7263. [CrossRef]
24. Zhao, L.; Huang, J.; Chen, J.; Ye, M. A Parallel Speed and Rotor Time Constant Identification Scheme for Indirect Field Oriented Induction Motor Drives. *IEEE Trans. Power Electron.* **2016**, *31*, 6494–6503. [CrossRef]
25. Perez, J.N.H.; Hernandez, O.S.; Caporal, R.M.; de J R Magdaleno, J.; Barreto, H.P. Parameter Identification of a Permanent Magnet Synchronous Machine based on Current Decay Test and Particle Swarm Optimization. *IEEE Lat. Am. Trans.* **2013**, *11*, 1176–1181. [CrossRef]
26. Krause, P.; Wasynczuk, O.; Sudhoff, S. *Analysis of Electric Machinery*; IEEE Press: Baltimore, MD, USA, 1995.
27. Mathew, S. *Wind Energy: Fundamentals, Resource Analysis and Economics*; Springer: Berlin, Germany, 2006.